ELSEVIER

Contents lists available at ScienceDirect

# **Results in Optics**

journal homepage: www.elsevier.com/locate/rio



# Field of view extension in Mueller matrix microscopy for whole-slide imaging of biological samples

Roman Demczylo a , Diego Silva b , Federico Lecumberry b , Ariel Fernández a , Federico Lecumberry b , Ariel Fernández

- <sup>a</sup> Instituto de Física, Facultad de Ingeniería, Universidad de la República, J. Herrera y Reissig 565, Montevideo, Uruguay
- b Instituto de Computación, Facultad de Ingeniería, Universidad de la República, J. Herrera y Reissig 565, Montevideo, Uruguay
- c Instituto de Ingeniería Eléctrica, Facultad de Ingeniería, Universidad de la República, J. Herrera y Reissig 565, Montevideo, Uruguay

# ARTICLE INFO

# Keywords: Polarized light microscopy Mueller matrix Whole slide imaging

#### ABSTRACT

Quantitative measures of the interaction of polarized light with tissue have been established as a powerful tool for biomedical diagnosis in recent years. In this regard, we implemented a microscopy setup that incorporates a polarized sensor in the imaging plane to obtain Stokes parameters corresponding to a given Field of View (FoV) of a tissue sample. By illuminating with linearly independent States of Polarization in the input, Mueller matrix elements can also be retrieved from the same FoV of the sample. In order to achieve whole-slide imaging the FoV can be extended by stitching multiple images taken after XY displacement. We propose introducing polarimetric features, specifically the Mueller matrix norm for each pixel, into the stitching algorithm. This allows for FoV extension with minimal overlap between neighboring images, substantially reducing the total number of images required for the entire sample. This approach can significantly reduce acquisition time and data storage requirements for whole-slide MM imaging. Validation results for the retrieval of whole-slide MM of tissue samples show SSIM =  $0.93 \pm 0.04$  and 100% stitching success from images with overlapping as low as 35%

#### 1. Introduction

The interaction of polarized light with tissue (Tuchin, 2016; He et al., 2021) constitutes a powerful tool to provide information about the structure of this biological material. The degree of depolarization of initially polarized light, the change in polarization state of incident light, and the polarization component that might be found in the output can all serve as indicators of the structural state of tissue sample.

Mueller matrix (MM) polarimetry (He et al., 2019; Qi and Elson, 2017; Shi et al., 2022) has recently been established as a valuable technique for the quantitative characterization of microstructural changes which represents an essential tool in diagnosis. Applications include, for example, cancer detection (Kupinski et al., 2018) or surgical imaging assistance (Qi et al., 2017).

The full,  $4 \times 4$  MM provides a comprehensive description of the polarization properties of a sample, derived from measurements utilizing both retarders and linear polarizers. However, reduced forms of the matrix (Chang et al., 2016; Novikova and Ramella-Roman, 2022) can still offer valuable information while reducing acquisition time and cost. For example, in the diagnosis of tissue pathology, relative changes in polarimetric parameters are often more significant than their

absolute values. In particular the  $3 \times 3$  MM (Demczylo and Fernández, 2024) can be obtained exclusively through linear measurements. Furthermore, the polar decomposition of this matrix (Swami et al., 2006) yields polarization parameters that require only linearly polarized input along with measurements with only linear polarizers.

Recent advances in sensing technology have also made microgrid polarizers integrated onto camera chips commercially available making real-time characterization of the State of Polarization (SoP) possible in Division of Focal Plane (DoFP) approximations (Sun et al., 2020; Hsu et al., 2015; Fernández and Demczylo, 2023). This new sensing technology allows to obtain linear Stokes parameters from a single shot after calibration of the system by means of the system matrix that maps the intensity measures on the sensor to the SoP of the input. Furthermore, polarization demosaicking schemes (Jiang et al., 2019; Gao and Gruev, 2011) might be applied to compensate for the loss of spatial resolution in these sensors in comparison to full-resolution in division of aperture methods (Llaguno et al., 2022).

A microscopy setup incorporating DoFP polarimetric sensing can then allow to obtain Stokes parameters corresponding to a given Field of View (FoV) of a sample of interest. By illuminating with linearly

E-mail address: arielfer@fing.edu.uy (A. Fernández).

<sup>\*</sup> Corresponding author.

<sup>&</sup>lt;sup>1</sup> The authors contributed equally to this work.

independent SoPs in the input, elements of the  $3 \times 3$  MM for a certain FoV of tissue sample can then be obtained with few measures over different linear SoPs in the ouput.

In order to retrieve features of interest over the complete sample, FoV extension to whole-slide imaging can be achieved through image stitching (Szeliski, 2022; Muhlich et al., 2022) of multiple images obtained for different regions of the same sample.

Image stitching is the image processing technique of combining multiple images with overlapping FoV into a single, larger, and more complete image (Muhlich et al., 2022; Schapiro et al., 2022). It combines several images, usually taken at high resolution, into a composite image with the images placed in the correct position, where the edges between images (seams) are imperceptible. This results in a final image that appears as a single capture, with a broader FoV and greater detail than its constituent parts (Madhusudana and Soundararajan, 2019).

Its most common applications are in photography and computer vision where it is used to create high-resolution panoramic images or to generate views with a wide FoV. However, with the study and development of this technique, its use has been extended to multiple areas. Document mosaicing, camera stabilization, satellite image mapping, and medical imaging are examples of its versatility (Wang and Yang, 2020).

In microscopy, stitching allows to join images from different areas of a sample provided certain conditions are met during capture, such as sufficient overlap. For example, the Fast and Robust Microscopic Image Stitching (FRMIS) (Mohammadi et al., 2024) algorithm presents a fast and robust method for stitching two overlapping images by considering only a subset of the features over the overlapping region. However, it relies solely on the intensity information of the sample, which may not always provide enough features to employ the stitching process.

In the present paper, a compact microscopy setup incorporating DoFP polarimetric sensing allows us to obtain  $3\times 3$  MM for a given FoV of the sample. Custom-built XY displacement allows for imaging over different regions of the sample with minimal mechanical error. Image stitching is performed following a novel technique in which we incorporate information derived from the MM for each pixel into the usual feature matching schemes. Comparison against state of the art techniques shows that our proposal allows for stitching with minimal overlapping between neighbor FoVs which in turn allows for whole-slide MM imaging with a minimal number of input images.

The paper is organized as follows. The basics of Stokes and Mueller calculus are introduced in Section 2. The optical setup is explained in Section 3.1, MM computation is devoted to Section 3.2 while FoV extension through image stitching is addressed in Section 3.3. Results and Discussion are presented in Section 4 while Conclusion can be found in Section 5.

# 2. Theory

Polarization is a fundamental property of light that describes the orientation of the electric field vector relative to its direction of propagation. The linear Stokes parameters are a set of three independent real values calculated as follows (Goldstein, 2017):

$$\begin{split} S_0 &= \frac{1}{2} \left( I^{0^\circ} + I^{90^\circ} + I^{45^\circ} + I^{-45^\circ} \right), \\ S_1 &= I^{0^\circ} - I^{90^\circ}, \\ S_2 &= I^{45^\circ} - I^{-45^\circ}, \end{split} \tag{1}$$

where  $I^{0^{\circ}}$ ,  $I^{45^{\circ}}$ ,  $I^{90^{\circ}}$ , and  $I^{-45^{\circ}}$  represent the intensity of light obtained after linear polarizers at  $0^{\circ}$ ,  $45^{\circ}$ ,  $90^{\circ}$ , and  $-45^{\circ}$ , respectively.

When a ray of light interacts with an object, its state of polarization undergoes a transformation that can be accounted for by means of a transfer function known as the Mueller matrix (MM). Using only linear input states of polarization and sensing with linear polarizers a  $3\times 3$  matrix M can be obtained. If  $\vec{S}_{in}=\begin{pmatrix} S_0 & S_1 & S_2 \end{pmatrix}^T$  is a linear input

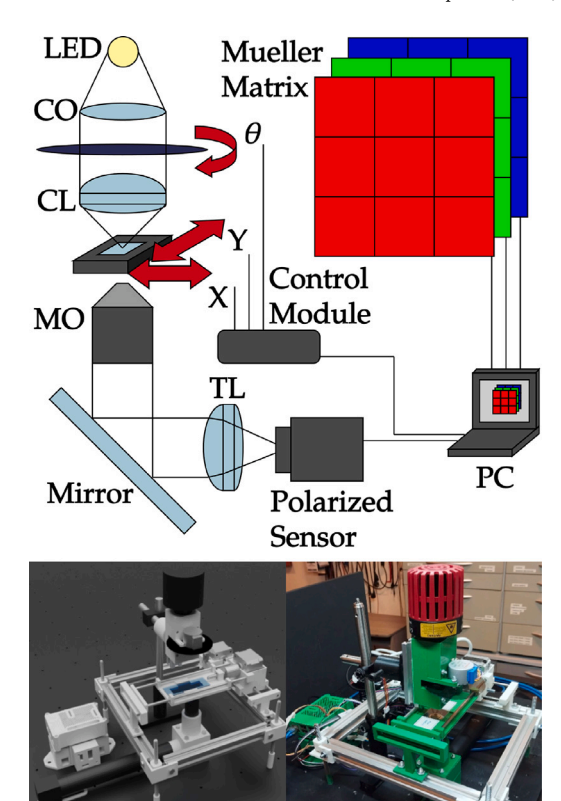


Fig. 1. Overview of the optical system design. Top: Scheme of the optical setup. CO: Collector Lens, CL: Condenser Lens, MO: Microscope Objective, TL: Tube Lens. Bottom left: Rendering of the 3D model designed in Blender. Bottom right: a picture of the real device (3D-printed case for Raspberry Pi and its modules adapted from huczekdesign (2023), VincentM (2017), ShmilCat (2023), juh (2020)).

state of polarization and  $\vec{S}_{out} = \begin{pmatrix} S_0' & S_1' & S_2' \end{pmatrix}^T$  is the output state of polarization, then

$$\vec{S}_{out} = \begin{pmatrix} S_0' \\ S_1' \\ S_2' \end{pmatrix} = \begin{pmatrix} m_{00} & m_{01} & m_{02} \\ m_{10} & m_{11} & m_{12} \\ m_{20} & m_{21} & m_{22} \end{pmatrix} \begin{pmatrix} S_0 \\ S_1 \\ S_2 \end{pmatrix} = \mathbf{M}\vec{S}_{in}.$$
 (2)

Given a set of integers,  $J=\{1,2,\ldots,N\}$  with  $N\geq 3$ , we define a sequence of N distinct linear input states of polarization, denoted as  $\{\vec{S}_{ij}^{(i)}\}_{i\in J}$ . Each element of the sequence is computed using the following equation:

$$\vec{S}_{in}^{(i)} = S_0(i) \left( 1 \quad \cos 2\theta_i \quad \sin 2\theta_i \right)^T, \tag{3}$$

where  $\theta_i$  is the angle of polarization for the Stokes vector. The corresponding set of output polarization states,  $\{\vec{S}_{out}^{(i)}\}_{i\in J}$ , is then related to the input polarization states by the use of (2), leading to the following expression:

$$\begin{bmatrix} \vec{S}_{out}^{(1)} & \cdots & \vec{S}_{out}^{(N)} \end{bmatrix} = \mathbf{M} \begin{bmatrix} \vec{S}_{in}^{(1)} & \cdots & \vec{S}_{in}^{(N)} \end{bmatrix}, \tag{4}$$

where M is the Mueller matrix. By pseudo-inversion of (4), the Mueller matrix can be retrieved as

$$\mathbf{M} = \begin{bmatrix} \vec{S}_{out}^{(1)} & \cdots & \vec{S}_{out}^{(N)} \end{bmatrix} \begin{bmatrix} \vec{S}_{in}^{(1)} & \cdots & \vec{S}_{in}^{(N)} \end{bmatrix}^{\dagger}, \tag{5}$$

where † is the pseudo-inverse (Moore–Penrose inverse).

Matrix M can be normalized by dividing each component by transmittance of the sample  $m_{00}$ :

$$\hat{\mathbf{M}} = \frac{1}{m_{00}} \mathbf{M}.\tag{6}$$

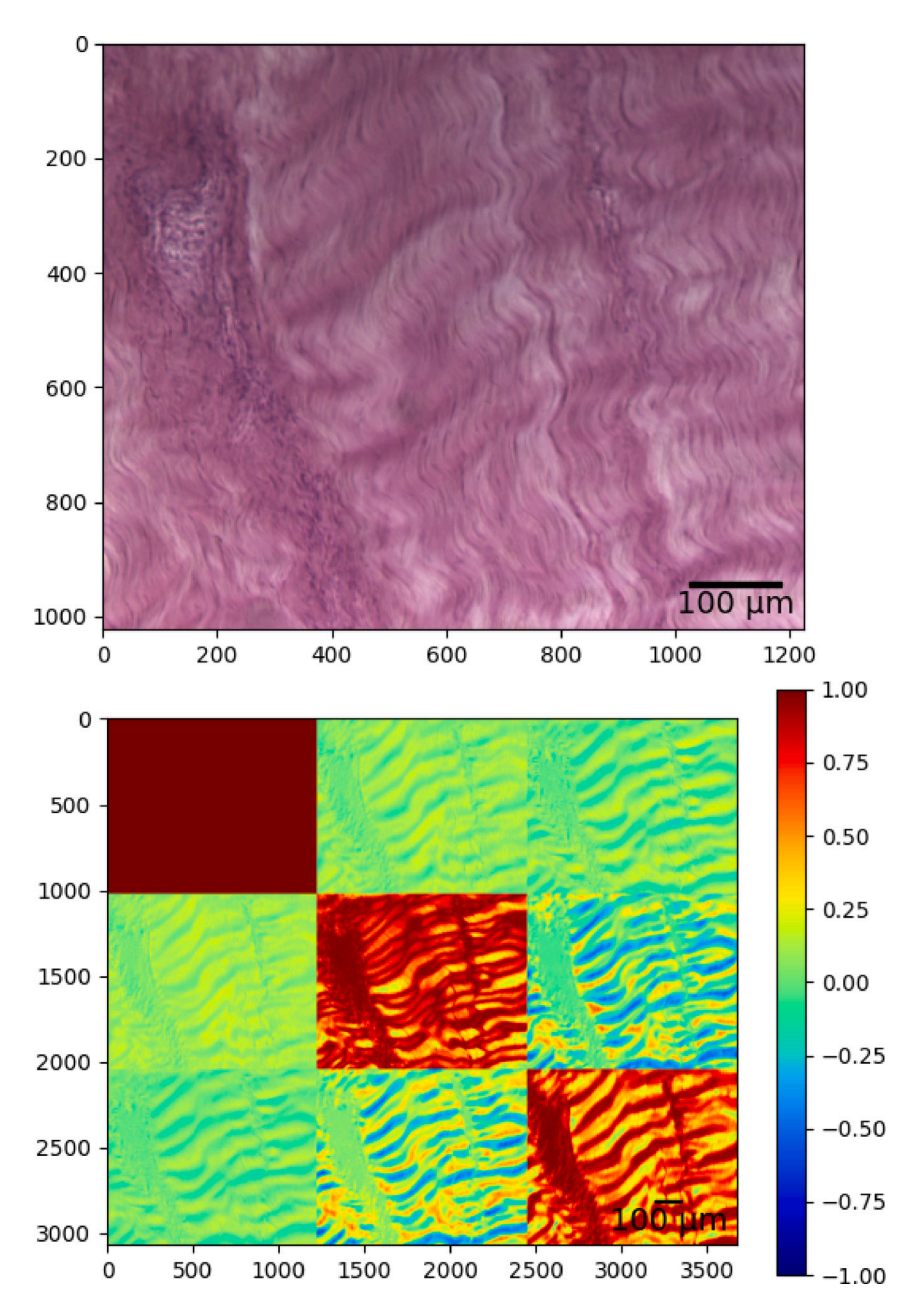


Fig. 2. Results of Mueller matrix calculus over tissue sample. Top: Transmittance of tissue sample,  $m_{00}$ . Bottom: Normalized Mueller matrix in the green channel,  $\hat{M}_G$ . Scale bar: 100 μm.

In order to proceed into FoV extension of the sample, matrix information is then codified into a single scalar which we chose to be the infinity norm of  $\hat{\mathbf{M}}$ :

$$\|\hat{\mathbf{M}}\|_{\infty} = \max_{0 \le i \le 2} \left\{ \sum_{j=0}^{2} |\hat{m}_{ij}| \right\}.$$
 (7)

# 3. Materials and methods

# 3.1. Optical setup

A schematic of our phase retrieval microscopy setup is shown in Fig. 1. The sample of interest (AmScope glass prepared dense connective tissue) is illuminated by a polarized white LED source. The sample is placed in front of a microscope objective (Olympus UPLFLN 10x, numerical aperture NA = 0.30, lateral resolution 1.1  $\mu m$ , focal length

 $f_{MO}=18$  mm, working distance WD = 10 mm) and at the conjugate image plane of a polarized color sensor (Sony IMX250MYR, 2448 × 2048 pixels resolution, 3.45 µm pixel pitch, quantum efficiency peaks for RGB pixels of 45%, 56% and 47% at 630, 525 and 470 nm, respectively) which allows for DoFP sensing. A color, four directional polarization image is then obtained in a single shot. Lateral magnification of the entire system, M, was estimated using a high-resolution microscopy target (Technologie Manufaktur, chromium [OD > 6 @ 550 nm] on fused silica,  $7.5-3300\ Lp/mm$ ), resulting in M=11.

Angle of polarization  $\theta$  of SoP in the input can be modified by means of a rotating polarizer motorized with a stepper motor  $(5,625^{\circ})$  step angle). The sample can be displaced in the XY directions by means of a motorized stage with two stepper motors  $(1.8^{\circ})$  step angle). A control module is employed to address the stepper motors the position defined by the 3-tuple  $(X,Y,\theta)$ . A PC drives in turn the controller and performs Mueller matrix calculation for each R, G, B channel and each (X,Y) position of the stage.

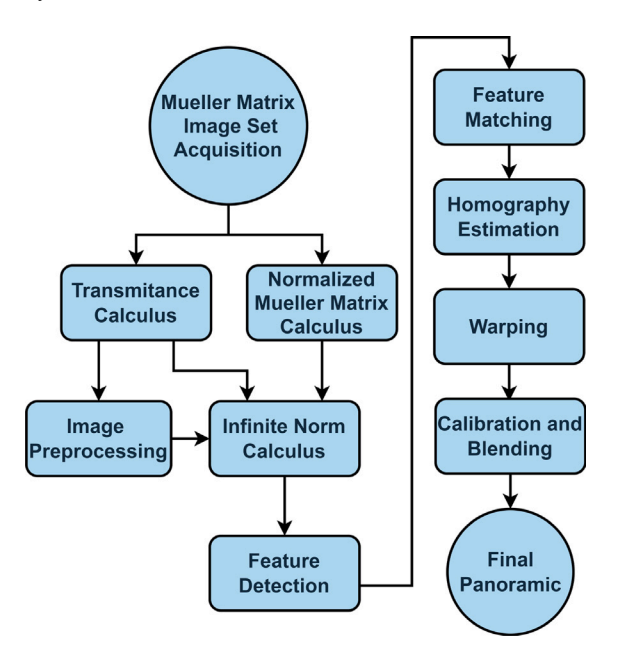
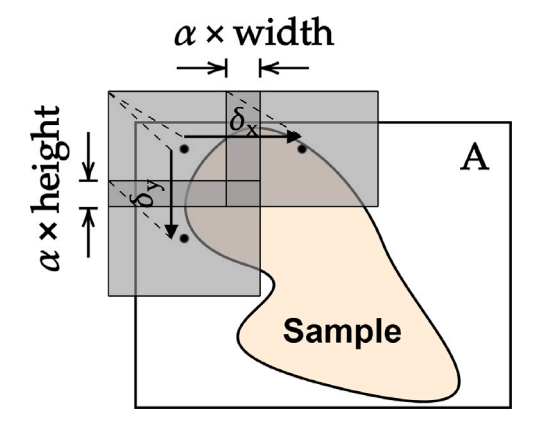


Fig. 3. Stitching algorithm flow diagram.



**Fig. 4.** Scheme of the acquisition procedure. The gray rectangle represents the FoV of the sensor projected onto the sample.

# 3.2. Mueller matrix computation

The aforementioned polarized sensor captures each polarized intensity image  $(I^{0^\circ}, I^{45^\circ}, I^{90^\circ})$ , and  $I^{-45^\circ})$  in real time by the means of the aforementioned polarized sensor. To accurately reconstruct the intensity for each corresponding color channel, a traditional demosaicing algorithm is required for each polarization direction. This process results in a subsampling of the original sensor dimensions by a factor of two so information of interest is obtained on a 2 × 2 superpixel basis. Defining the intensity vector as  $\vec{I}(x,y,\lambda) = \begin{pmatrix} I^{0^\circ} & I^{45^\circ} & I^{90^\circ} & I^{-45^\circ} \end{pmatrix}^T(x,y,\lambda)$  the Stokes vector  $\vec{S}(x,y,\lambda) = \begin{pmatrix} S_0 & S_1 & S_2 \end{pmatrix}^T(x,y,\lambda)$ , can be obtained for each superpixel (x,y) and each color channel  $\lambda = R, G, B$  by pseudo-inverting the following equation:

$$\vec{I}(x, y, \lambda) = A\vec{S}(x, y, \lambda), \tag{8}$$

where transfer matrix  $\bf A$  incorporates effects due to non ideal transmission and or orientation angles of the microgrid polarizers of the sensor as well as the pixel dark current. The in detail study of the polarized sensor employed in this work (see Lane et al. (2022)) shows that there is no significant spatial variation of the transfer matrix and dark current effect is negligible. Besides, given extinction ratios > 300

for the microgrid polarizers, the transfer matrix can be approximated by its ideal form:

$$\mathbf{A} = \frac{1}{2} \begin{pmatrix} 1 & 1 & 0 \\ 1 & 0 & 1 \\ 1 & -1 & 0 \\ 1 & 0 & -1 \end{pmatrix}. \tag{9}$$

A set of N=6 input polarization states with angle of polarization of  $0^{\circ}$ ,  $30^{\circ}$ ,  $60^{\circ}$ ,  $90^{\circ}$ ,  $120^{\circ}$  and  $150^{\circ}$  was employed. The Mueller matrix over the field of view of the polarized sensor on each color channel can be computed by means of Eq. (5), leading to the following equation:

$$\mathbf{M}(x, y, \lambda) = \begin{bmatrix} \vec{S}_{out}^{(1)} & \cdots & \vec{S}_{out}^{(N)} \end{bmatrix} \begin{bmatrix} \vec{S}_{in}^{(1)} & \cdots & \vec{S}_{in}^{(N)} \end{bmatrix}^{\dagger} (x, y, \lambda).$$
 (10)

The input Stokes vectors on the r.h.s. of Eq. (10) are obtained for the system in the absence of sample and their pseudo-inverse can be calculated one time and saved for Mueller matrix retrieval over any stage position assuming consistent rotational settings for the motorized polarizer. After the output Stokes vectors are acquired Mueller matrix can be efficiently calculated using the *einsum* algorithm provided by the NumPy library in Python. An example of a Mueller matrix calculus over a section of the tissue sample is shown in Fig. 2.

#### 3.3. Field of view extension

Building a tile image by stitching several limited FoV images imposes challenges related to the variability that may exist from one image to another (perspective, exposure, rotation, etc.). Additionally, the limited information that may exist in a set of images is an obstacle, being the presence of overlapping between images one of the essential requirements to achieve tile images with good quality. Other important issues that need to be taken into account are the presence of parallax, lens distortion, and scene motion. The goal of a stitching algorithm is to produce a visually plausible mosaic with two desirable properties. First, the mosaic should be as close to the input images as possible both in terms of geometry and intensity distribution. Second, the seam between the assembled images should be imperceptible. In our case, a feature-based stitching method is implemented.

Typically, a feature-based stitching algorithm can be summarized in six major steps: preprocessing, feature detection, feature matching, homography estimation, warping, and blending (Adel et al., 2014). The novelty of our proposal lies in the use of polarimetric properties of the sample that enhance feature visibility. In particular, for each input image the infinite norm of the Mueller matrix is calculated and represented as a new image, resulting in a new set of characteristics. This set is then used for adjusting parameters of a state of the art stitching algorithm in order to finally stitch the transmittance input image set. Using the open source library 'Open Stitching' (Weber, 2022), based on the OpenCV stitching module, we developed Python functions corresponding to each step of the stitching algorithm, enabling efficient handling of our samples. This process is illustrated in Fig. 3.

#### 3.3.1. Image acquisition

The first step in a successful stitching process is obtaining a suitable set of images. A schematic procedure for image acquisition of a sample is shown in Fig. 4. The degree  $\alpha$  of overlap between neighbor images is useful in determining the number of images required to fully capture the entire tissue sample. A larger overlap parameter  $\alpha$  increases both the number of images and the time required to complete the acquisition of the entire sample.

The FoV of the system can be obtained in terms of the width (W) and height (H) of the sensor as seen on the object plane:

$$FoV = W \times H, \ W = \frac{N_x \times p}{M}, \ H = \frac{N_y \times p}{M}, \ \ (11)$$

where  $N_x=2448$  is the horizontal pixel resolution,  $N_y=2048$  is the vertical pixel resolution,  $p=3.45~\mu m$  the pixel pitch of the sensor

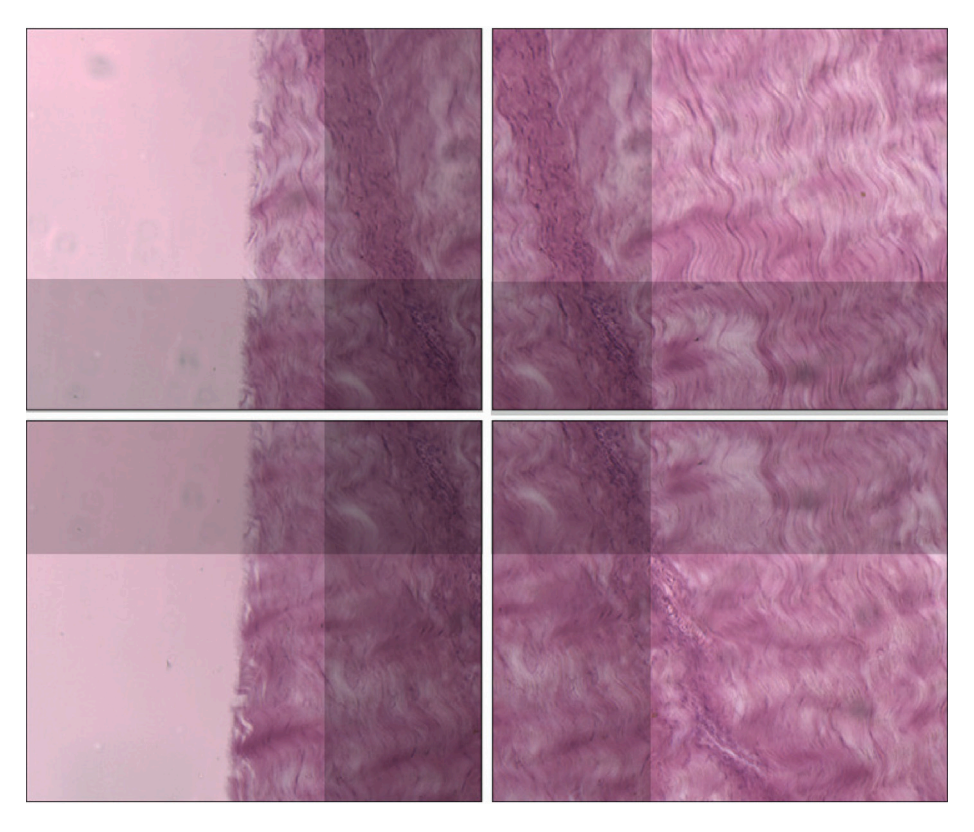


Fig. 5. Set of transmittance images of tissue sample with 35% overlap (overlap area highlighted in gray in each image).

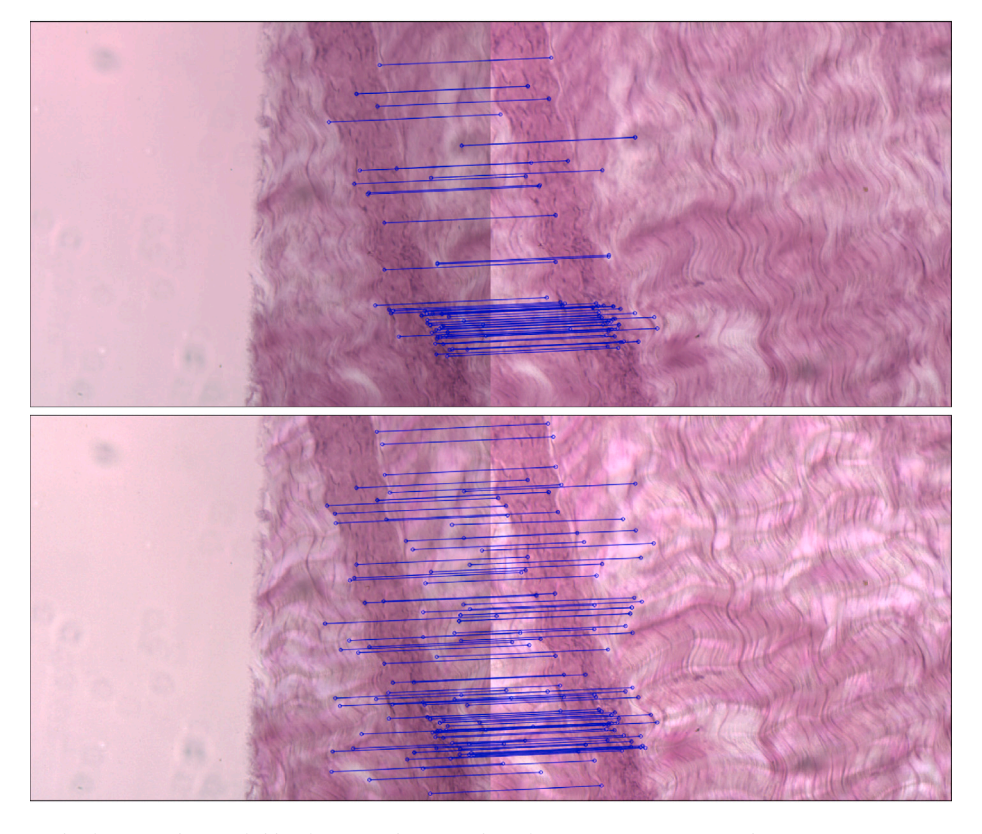


Fig. 6. Feature matching results for two adjacent fields of view with an overlap of 35%. Top: Feature matching on transmittance image set. Bottom: Feature matching on infinite norm Mueller matrix image set.

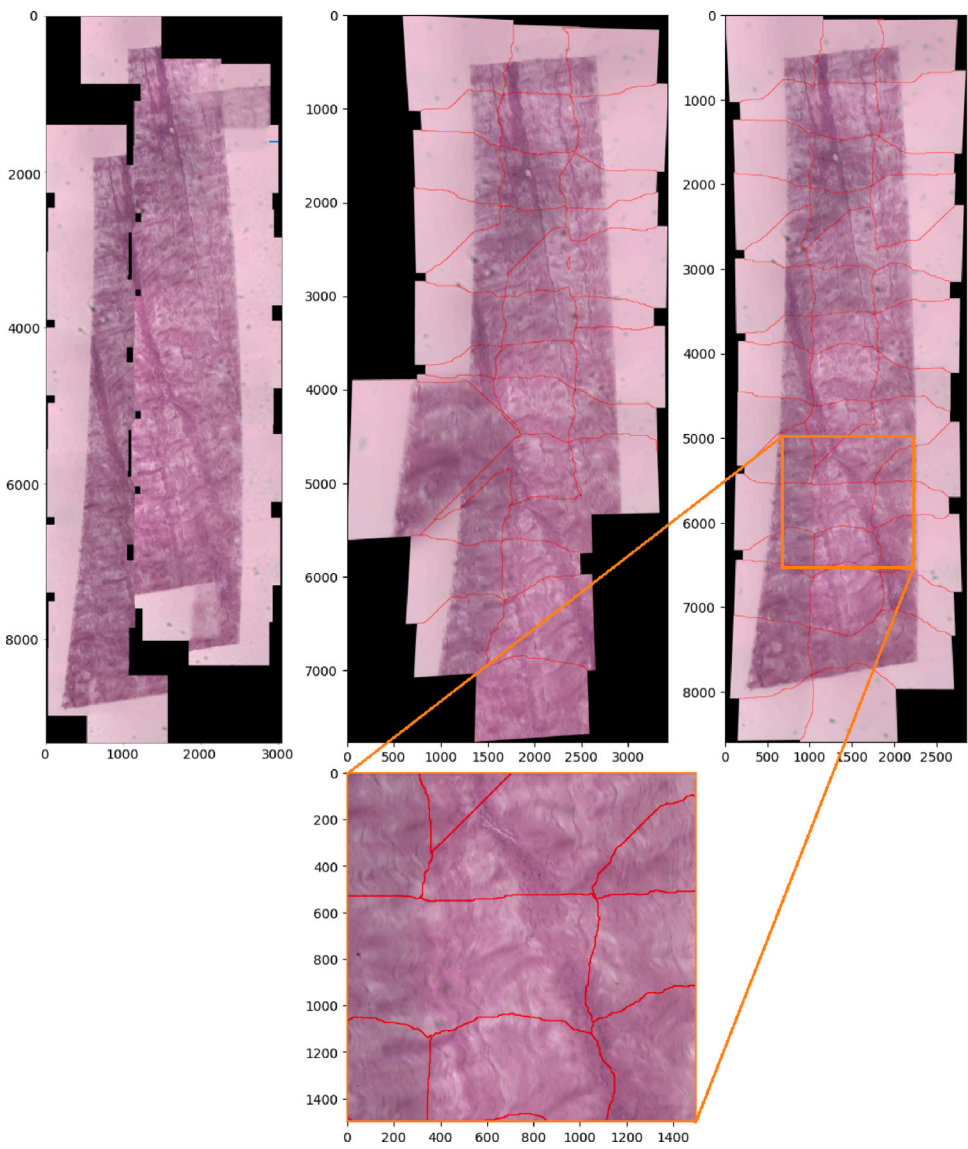


Fig. 7. Top left: Stitched transmittance maps obtained using Fiji's method. Top center: Stitched transmittance maps obtained using Python's transmittance based method. Top right: Stitched transmittance maps obtained using the Mueller matrix based method. Bottom: Zoomed-in view of the area highlighted by the orange square.

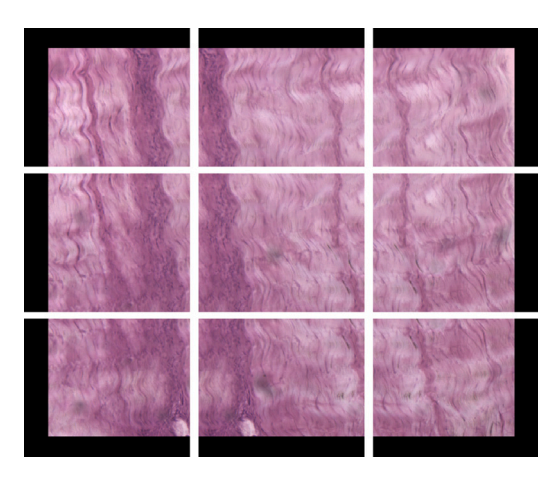


Fig. 8. Example of transmittance from an image of the subset divided into overlapping sections ( $n_S=9,~\alpha=0.35$ ).

and M=11 the lateral magnification of the system. To achieve the desired overlap, stage must be displaced in X and Y directions by  $\delta_x=(1-\alpha)W$  and  $\delta_y=(1-\alpha)H$ , respectively, as illustrated in Fig. 4. Hence, assuming that the tissue sample is completely enclosed within a rectangular bounding box of area A, the total number of images required to cover the entire sample can be calculated as:

$$N = \left\lceil \frac{A}{\delta_x \delta_y} \right\rceil = \left\lceil \frac{A}{(1 - \alpha)^2 \times FoV} \right\rceil,\tag{12}$$

where  $\lceil x \rceil$  represents the ceil function of x (lowest integer greater than x). For our proof of concept experiments where the tissue sample fits within an area  $A \approx 9 \text{ mm}^2$ , overlap parameter  $\alpha = 0.35$  requires N = 44 images to completely cover the sample area while  $\alpha = 0.5$  increases the number of required images to 73.

An example of input images with overlap parameter  $\alpha=0.35$  is illustrated in Fig. 5.

### 3.3.2. Infinite norm computation

Instead of feature extraction based only on transmittance,  $m_{00}(x, y, \lambda)$ , we propose an alternative method based on feature extraction from the infinity norm of the Mueller matrix,  $\mathbf{M}(x, y, \lambda)$ , computed as follows:

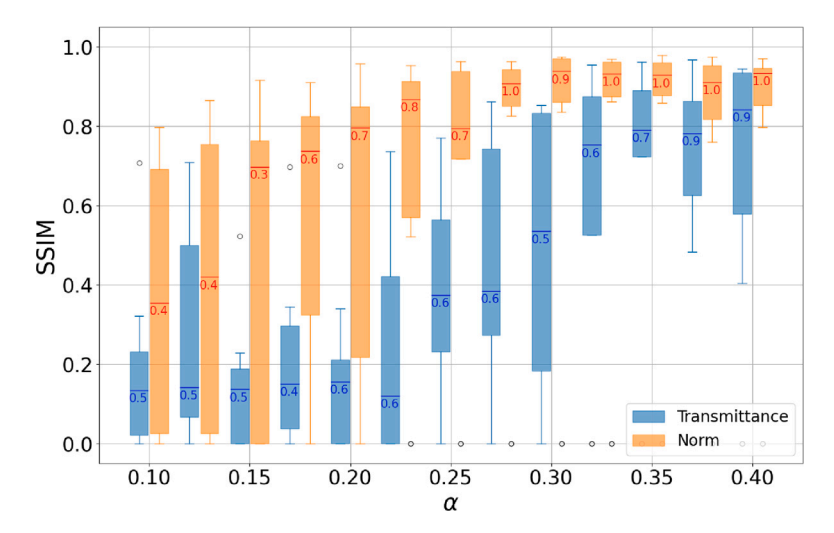


Fig. 9. Boxplot of the SSIM over n = 10 different stitched transmittance images and stitched infinite norm Mueller matrix images for each overlap  $\alpha$  across the tissue sample. The number inside each boxplot represents the ratio of sections that were successfully stitched.

Table 1 SSIM confidence interval for both methods and for each overlap  $\alpha$ .

α	Transmittance method			Mueller method		
	Mean	STD	Success	Mean	STD	Success
0.1	0.2691	0.2364	50%	0.5562	0.2711	40%
0.125	0.3967	0.2527	50%	0.6157	0.2996	40%
0.15	0.2070	0.1741	50%	0.7916	0.0915	30%
0.175	0.3353	0.2235	40%	0.7480	0.1562	60%
0.2	0.2530	0.2226	60%	0.7628	0.2296	70%
0.225	0.3289	0.2792	60%	0.8358	0.1377	80%
0.25	0.5149	0.1881	60%	0.8544	0.0887	70%
0.275	0.5829	0.2100	50%	0.9106	0.0428	100%
0.3	0.6834	0.1956	60%	0.9366	0.0451	90%
0.325	0.8213	0.0918	70%	0.9315	0.0376	100%
0.35	0.8465	0.0822	90%	0.9345	0.0373	100%
0.375	0.8036	0.1297	90%	0.9071	0.0660	100%
0.4	0.8232	0.1609	90%	0.9212	0.0485	100%

$$\|\mathbf{M}\|_{\infty}(x, y, \lambda) = \max_{0 \le i \le 2} \left\{ \sum_{j=0}^{2} |m_{ij}(x, y, \lambda)| \right\}$$
  
=  $m_{00}(x, y, \lambda) \|\hat{\mathbf{M}}\|_{\infty}(x, y, \lambda).$  (13)

Intuitively, the infinity norm of the normalized Mueller matrix,  $\|\hat{\mathbf{M}}\|_{\infty}(x,y,\lambda)$ , acts as a mask with bounded values that enhances the features of the transmittance map,  $m_{00}(x,y,\lambda)$ , making it easier to stitch. By applying the infinite norm of the Mueller matrix to each element in our dataset, we produce a set of images that can be directly fed into a state of the art stitching algorithm without any further modifications.

#### 3.3.3. Feature detection

Interest points and descriptors (corners, edges, etc.) are identified in each image of the infinite norm Mueller matrix set. The SIFT (Scale-Invariant Feature Transform) algorithm (Lowe, 1999) is often most effective at this stage. It describes the local appearance around each keypoint in a way that is ideally invariant to illumination, translation, scale, and rotation, producing a descriptor vector for each keypoint. Thus, detection can be divided into keypoint identification and description.

#### 3.3.4. Feature matching

Features between pairs of images are compared to find correspondences in overlapping areas. This can be achieved using algorithms like ORB (Oriented FAST and Rotated BRIEF) (Rublee et al., 2011), SIFT, or SURF (Speeded Up Robust Features) (Bay et al., 2008) for feature

detection and matching key points. Next, we determine which images are the best based on the matches using a confidence threshold for the matching score. This process results in a subset that contains only the relevant images. A display of the results for this step is shown in Fig. 6, which compares the results using the transmittance set of images with those obtained from the infinite norm Mueller matrix set of images. This comparison demonstrates how the Mueller matrix can improve feature matching.

#### 3.3.5. Homography estimation and warping

Feature correspondences are used to calculate the homography that describes the geometric transformation (rotation, scaling, translation) needed to align the images. Before we can align images, we need to establish mathematical relationships that map the pixel coordinates of one image to another. Homography is a projective transformation that determines the correspondence between two planar geometric figures (Szeliski, 2006). This allows us to map points in one image to their corresponding points in another image. As a result, it becomes possible to align and register images taken from different perspectives or with different cameras by estimating a transformation that converts a region of one image into a region of another image. This is the last procedure to be applied on the infinite norm Mueller matrix image set. Subsequently, warping is performed on the images from the transmittance image set, involving the application of the estimated homography to each image in order to map its pixels from their locations in the source image to their corresponding locations in the final panoramic image.

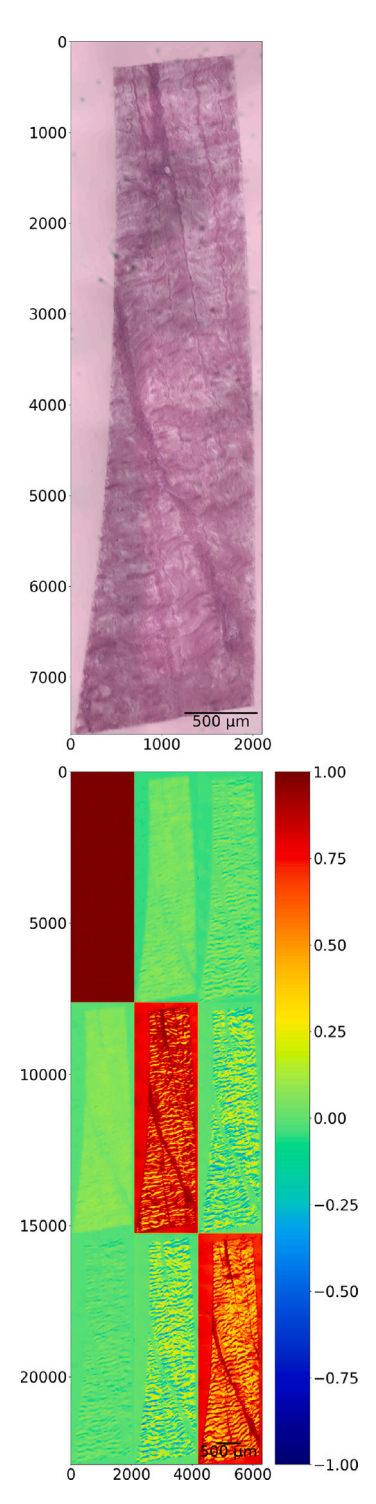


**Fig. 10.** Results of Mueller matrix calculus over the entire tissue sample. Top: Transmittance of tissue sample,  $m_{00}$ . Bottom: Normalized Mueller matrix in the green channel,  $\hat{M}_G$ . Scale bar: 500 μm.

#### 3.3.6. Calibration and blending

Image parameters are corrected to minimize differences (such as exposure variations or color inconsistencies), and aligned images are blended to create a single seamless panoramic image. The seam path is calculated to correspond to the optimal path to minimize overlap error (Efros and Freeman, 2023).

In order to compare our approach with a traditional stitching method, we applied Fiji's "Grid/Collection stitching" plugin to the same

transmittance dataset. A comparison between Fiji's results and those obtained with the other two Python-based methods — using either transmittance or the Mueller-matrix-derived feature — is presented in Fig. 7, where stitching seams are highlighted in red for illustration.

#### 4. Results and discussion

Fiji's method completed the stitching in less than one minute, while the other two Python-based methods required approximately twenty minutes. However, as shown in Fig. 7, the blended seams in Fiji's result are misaligned and some crops are missing. Python's transmittance-based method achieves better seam alignment, although it introduces some curvature and cannot stitch all patches. In contrast, our Mueller-based method successfully stitches all the dataset, providing better global alignment and blending.

In order to assess the effectiveness of our approach we select a subset of n=10 images from our dataset which will serve as ground truth in the following. Each image of the subset is divided into  $n_S=9$  overlapping sections with overlap  $\alpha$  ranging from 0.1 to 0.4 in increments of 0.025. An example of image cropping with  $\alpha=0.35$  is shown in Fig. 8. This sample corresponds to the tissue area captured within the camera's field of view (FoV). The crops are artificially generated and used as ground truth for the experiment. Therefore, regions outside the field of view (FoV) are represented with a black color.

For every overlap value  $\alpha$  the  $n_S$  sections of each image are stitched using both methods: the traditional approach based on the transmittance of the sample and our method based on the infinite norm of the Mueller matrix. The mean and standard deviation (over n = 10realizations of the experiment) of the structural similarity index (SSIM) computed between the stitched image and the original image across the selected images for each value of  $\alpha$ , are presented as boxplots in Fig. 9. Table 1 summarizes the numerical results of the experiments together with the stitching success rate, defined as the percentage of image crops that were successfully aligned into the panorama. Our approach clearly enhances the features of the images, improving the stitching process and overall performance. For  $\alpha = 0.35$  the proposed method allows to obtain a resulting image with SSIM =  $0.93 \pm 0.04$ and all the sections successfully stitching. Please note that for the same overlap the transmittance approach only allows for 70% success ratio and a significantly lower structural similarity SSIM =  $0.84 \pm 0.08$ .

The homography matrices obtained using the infinite norm of the Mueller matrix can be applied to stitch each normalized Mueller matrix component, along with the transmittance image of the sample, using the images captured over the entire tissue sample with the mechanical stage. Since both the transmittance and the Mueller matrix are computed in parallel, they share the same spatial geometry and therefore the same homography transformations. Results for the whole-slide Mueller matrix, composed of N=44 images of a tissue sample in the green channel, as well as the corresponding whole-slide transmittance image, are presented in Fig. 10.

#### 5. Conclusion

We have shown through a series of experiments that incorporating the infinite norm of the Mueller matrix of a sample allows for image stitching (both of the regular transmittance image and Mueller matrix components) from limited FoV images acquired with a compact polarization microscope. The resulting images preserve the lateral resolution of the acquired ones and also allow to explore the sample at different scales

Comparison against state of the art techniques by means of Structural Similarity Index Measure (SSIM) shows that our proposal allows for whole slide imaging with SSIM =  $0.93 \pm 0.04$  and 100% stitching success from images with overlapping as low as 35%, outperforming approaches based solely in transmittance image of the sample.

As a future line of work we consider combining the obtained results with other techniques like auto-fluorescence imaging in order to allow for whole-slide multimodal microscopy.

#### CRediT authorship contribution statement

Roman Demczylo: Writing – review & editing, Writing – original draft, Validation, Software, Methodology, Investigation, Formal analysis, Data curation. Diego Silva: Writing – review & editing, Writing – original draft, Software, Investigation, Data curation. Federico Lecumberry: Writing – review & editing, Validation, Supervision, Software. Ariel Fernández: Writing – review & editing, Writing – original draft, Supervision, Project administration, Methodology, Investigation, Formal analysis, Conceptualization.

#### Declaration of competing interest

The authors declare that they have no known competing financial interests or personal relationships that could have appeared to influence the work reported in this paper.

### Acknowledgment

This work is supported by Comisión Sectorial de Investigación Científica (22520240100040UD).

#### Data availability

Data will be made available on request.

#### References

- Adel, Ebtsam, Elmogy, Mohammed, El-Bakry, Hazem, 2014. Image stitching based on feature extraction techniques: A survey. Int. J. Comput. Appl. 99, 1–8.
- Bay, Herbert, Ess, Andreas, Tuytelaars, Tinne, Van Gool, Luc, 2008. Speeded-up robust features (SURF). Comput. Vis. Image Underst. 110 (3), 346–359.
- Chang, Jintao, He, Honghui, Wang, Ye, Huang, Yi, Li, Xianpeng, He, Chao, Liao, Ran, Zeng, Nan, Liu, Shaoxiong, Ma, Hui, 2016. Division of focal plane polarimeter-based 3× 4 mueller matrix microscope: a potential tool for quick diagnosis of human carcinoma tissues. J. Biomed. Opt. 21 (5), 056002–056002.
- Demczylo, Roman, Fernández, Ariel, 2024. Single-shot  $3\times 3$  mueller matrix microscopy with color polarization encoding. Opt. Lett. 49 (23), 6829–6832.
- Efros, Alexei A., Freeman, William T., 2023. Image quilting for texture synthesis and transfer, first ed. In: Seminal Graphics Papers: Pushing the Boundaries, vol. 2, Association for Computing Machinery, New York, NY, USA.
- Fernández, Ariel, Demczylo, Roman, 2023. Real-time polarimetric microscopy of biological tissue. In: Novel Techniques in Microscopy. Optical Society of America, pp. NW1C-2.
- Gao, Shengkui, Gruev, Viktor, 2011. Bilinear and bicubic interpolation methods for division of focal plane polarimeters. Opt. Express 19 (27), 26161–26173.
- Goldstein, Dennis H., 2017. Polarized Light. CRC Press.
- He, Chao, He, Honghui, Chang, Jintao, Chen, Binguo, Ma, Hui, Booth, Martin J., 2021.Polarisation optics for biomedical and clinical applications: a review. Light.: Sci. Appl. 10 (1), 1–20.
- He, Honghui, Liao, Ran, Zeng, Nan, Li, Pengcheng, Chen, Zhenhua, Liu, Xi, Ma, Hui, 2019. Mueller matrix polarimetry—an emerging new tool for characterizing the microstructural feature of complex biological specimen. J. Lightwave Technol. 37 (11), 2534–2548.
- Hsu, Wei-Liang, Davis, Jeffrey, Balakrishnan, Kaushik, Ibn-Elhaj, Mohammed, Kroto, Shona, Brock, Neal, Pau, Stanley, 2015. Polarization microscope using a near infrared full-Stokes imaging polarimeter. Opt. Express 23 (4), 4357–4368.

- huczekdesign, 2023. Raspberry Pi Case, https://www.printables.com/es/model/219727-raspberry-pi-case.
- Jiang, Tuochi, Wen, Desheng, Song, Zongxi, Zhang, Weikang, Li, Zhixin, Wei, Xin, Liu, Gang, 2019. Minimized Laplacian residual interpolation for DoFP polarization image demosaicking. Appl. Opt. 58 (27), 7367–7374.
- juh, 2020. Nema17 Case, https://www.thingiverse.com/thing:3269804.
- Kupinski, Meredith, Boffety, Matthieu, Goudail, François, Ossikovski, Razvigor, Pierangelo, Angelo, Rehbinder, Jean, Vizet, Jérémy, Novikova, Tatiana, 2018. Polarimetric measurement utility for pre-cancer detection from uterine cervix specimens. Biomed. Opt. Express 9 (11), 5691–5702.
- Lane, Connor, Rode, David, Rösgen, Thomas, 2022. Calibration of a polarization image sensor and investigation of influencing factors. Appl. Opt. 61 (6), C37–C45.
- Llaguno, Juan M., Lecumberry, Federico, Fernández, Ariel, 2022. Snapshot polarimetric imaging in multi-view microscopy. Appl. Opt. 61 (9), F62–F69.
- Lowe, David G., 1999. Object recognition from local scale-invariant features. In: Proceedings of the Seventh IEEE International Conference on Computer Vision, vol. 2, Ieee, pp. 1150–1157.
- Madhusudana, Pavan Chennagiri, Soundararajan, Rajiv, 2019. Subjective and objective quality assessment of stitched images for virtual reality. IEEE Trans. Image Process. 28 (11), 5620–5635.
- Mohammadi, F.S., Shabani, H., Zarei, M., 2024. Fast and robust feature-based stitching algorithm for microscopic images. Sci. Rep. 14 (1), 13304.
- Muhlich, Jeremy L., Chen, Yu-An, Yapp, Clarence, Russell, Douglas, Santagata, Sandro, Sorger, Peter K., 2022. Stitching and registering highly multiplexed whole-slide images of tissues and tumors using ASHLAR. Bioinformatics 38 (19), 4613–4621.
- Novikova, Tatiana, Ramella-Roman, Jessica C., 2022. Is a complete mueller matrix necessary in biomedical imaging? Opt. Lett. 47 (21), 5549–5552.
- Qi, Ji, Elson, Daniel S., 2017. Mueller polarimetric imaging for surgical and diagnostic applications: a review. J. Biophotonics 10 (8), 950–982.
- Qi, Ji, He, Chao, Elson, Daniel S., 2017. Real time complete Stokes polarimetric imager based on a linear polarizer array camera for tissue polarimetric imaging. Biomed. Opt. Express 8 (11), 4933–4946.
- Rublee, Ethan, Rabaud, Vincent, Konolige, Kurt, Bradski, Gary, 2011. ORB: An efficient alternative to SIFT or SURF. In: 2011 International Conference on Computer Vision. Ieee, pp. 2564–2571.
- Schapiro, Denis, Sokolov, Artem, Yapp, Clarence, Chen, Yu-An, Muhlich, Jeremy, Hess, Joshua, Creason, Allison, Nirmal, Ajit, Baker, Gregory, Nariya, Maulik, Lin, Jia-Ren, Maliga, Zoltan, Jacobson, Connor, Hodgman, Matthew, Ruokonen, Juha, Farhi, Samouil, Abbondanza, Domenic, McKinley, Eliot, Persson, Daniel, Sorger, Peter, 2022. MCMICRO: a scalable, modular image-processing pipeline for multiplexed tissue imaging. Nature Methods 19.
- Shi, Yixuan, Chen, Binguo, He, Honghui, Ma, Hui, 2022. Quantitative assessment of tissue structures based on Mueller matrix polarimetry and derived parameters imaging. In: Polarized Light and Optical Angular Momentum for Biomedical Diagnostics 2022, vol. 11963, SPIE, International Society for Optics and Photonics, p. 119630C.
- ShmilCat, 2023. L298N driver case, https://www.printables.com/es/model/472016-double-1298n-case-with-zip-tie-closure-and-screw-h.
- Sun, Xueqian, Sun, He, Wang, Dejiang, Wang, Rui, Cheng, Chen, Zhang, Tao, 2020.
  Extinction ratio and image accuracy of relayed-microgrid polarimetric imaging systems: theory and experiment. Appl. Opt. 59 (8), 2298–2307.
- Swami, M.K., Manhas, S., Buddhiwant, P., Ghosh, N., Uppal, A., Gupta, P.K., 2006. Polar decomposition of 3x 3 Mueller matrix: a tool for quantitative tissue polarimetry. Opt. Express 14 (20), 9324–9337.
- Szeliski, Richard, 2006. Image alignment and stitching: A tutorial. Found. Trends Comput. Graph. Vis. 2.
- Szeliski, Richard, 2022. Computer Vision: Algorithms and Applications. Springer Nature.
- Tuchin, Valery V., 2016. Polarized light interaction with tissues. J. Biomed. Opt. 21 (7), 071114.
- VincentM, 2017. ULN2003 Case, https://www.thingiverse.com/thing:2317662.
- Wang, Zhaobin, Yang, Zekun, 2020. Review on image-stitching techniques. Multimedia Syst. 26.
- Weber, Lukas, 2022. Open Stitching, GitHub, https://github.com/OpenStitching/stitching.